

*Reprinted from*

JAPANESE JOURNAL OF  
**APPLIED  
PHYSICS**

**REGULAR PAPER**

**Detection of Boundaries of Carotid Arterial Wall by Analyzing Ultrasonic RF Signals**

Nabilah Ibrahim, Hideyuki Hasegawa, and Hiroshi Kanai

Jpn. J. Appl. Phys. **51** (2012) 07GF07

## Detection of Boundaries of Carotid Arterial Wall by Analyzing Ultrasonic RF Signals

Nabilah Ibrahim<sup>1</sup>, Hideyuki Hasegawa<sup>1,2</sup>, and Hiroshi Kanai<sup>1,2\*</sup>

<sup>1</sup>Graduate School of Engineering, Tohoku University, Sendai 980-8579, Japan

<sup>2</sup>Graduate School of Biomedical Engineering, Tohoku University, Sendai 980-8579, Japan

Received November 18, 2011; accepted January 10, 2012; published online July 20, 2012

In line with the fact that the intima–media thickness (IMT) of the carotid arterial wall is the most frequently used indicator to diagnose atherosclerosis by ultrasound, it is essential to accurately estimate the thickness of the intima–media complex (IMC) boundaries, i.e., the lumen–intima boundary (LIB) and media–adventitia boundary (MAB). In this study, an improved adaptive model of an ultrasonic echo was developed for the model to realize better fitting to the reference RF echo, which is measured from a glass plate, using a Gaussian window for the envelope function of the adaptive model. Using the mean squared error (MSE) method, the envelope of the improved adaptive model (multiply the sinusoidal wave with the Gaussian window) was fitted with the envelope of an RF echo measured *in vivo* to estimate the boundaries of the carotid arterial wall. Firstly, a computer simulation of the carotid arterial wall was conducted to evaluate the accuracy of boundary detection using the envelope of the improved adaptive model. In the simulation, IMT was set at 0.50 mm in a 7.2-mm-long short segment in the longitudinal direction. The IMT estimated by the proposed method was 0.54 mm. The 8% error between the true and detected IMTs showed the high accuracy of the envelope of the improved adaptive model in boundary detection. In the *in vivo* measurement, for the 4.8-mm-long short segment in the longitudinal direction, the average IMT automatically estimated by the proposed method was 0.57 mm. The result was compared with those obtained by the previous method and manually. The IMT estimated by the previous method, which uses an RF adaptive model, was 0.59 mm and the manually determined IMT was 0.56 mm. The smaller difference between the results obtained by the proposed method and manually verified that boundary detection by the proposed method was better than that by the previous method. © 2012 The Japan Society of Applied Physics

### 1. Introduction

Cardiovascular diseases are responsible for over 17.3 million deaths yearly and are the leading causes of death in the world.<sup>1)</sup> Moreover, in 2008, out of the 17.3 million cardiovascular deaths, 7.3 million were caused by heart attack and 6.2 million were caused by stroke. The rise in the prevalence of atherosclerosis or obesity is considered the main cause of cardiovascular diseases.<sup>2–4)</sup> Hence, the assessment of the risk of atherosclerosis and its diagnosis at an early stage have become very important. Early-stage atherosclerosis changes the structure of vessels and arteries, where smooth muscle cells in media (middle layer of the arterial wall) are associated with atherosclerosis lesions.<sup>5)</sup> The migration of smooth muscle cells to the intima (innermost layer of the arterial wall) also occurs, resulting in the thickening of the arterial wall. As a result, blood vessels constrict and the risk of cardiovascular diseases increase. Parallel to the fact that the intima–media thickness (IMT) of the carotid arterial wall is the most frequently used indicator to diagnose atherosclerosis by ultrasound,<sup>6)</sup> it is essential to accurately estimate the intima–media complex (IMC) boundaries, i.e., the lumen–intima boundary (LIB) and media–adventitia boundary (MAB). Additionally, Davis *et al.*<sup>7)</sup> have reported that IMT measurement in the carotid artery is more reproducible than the IMT measurement in the abdominal aorta because of the smaller amount of tissue between the ultrasonic probe and the carotid arterial wall.

Various techniques for detecting the boundaries and estimating the IMT have been proposed.<sup>5–14)</sup> Invasive and manual techniques for boundary detection<sup>8,9)</sup> are not desirable because the former requires surgical operation and the latter lacks reproducibility. Thus, noninvasive and automated techniques are necessary.<sup>10–14)</sup> Standard medical imaging tools such as computed tomography (CT) and magnetic resonance imaging (MRI) are widely used for the assessment of the IMT because they produce images with good spatial resolution. Boussel *et al.*<sup>10)</sup> compared the

measurement of the IMT and thickening of the carotid wall using MRI with that using ultrasound and found a very good agreement in results between these techniques. However, the method using MRI is time-consuming and cost-ineffective compared with that using ultrasound. Because ultrasonic devices are inexpensive, portable, and provides real-time results, IMT measured by the ultrasonic technique is more practical. Savithri and Purushothaman<sup>11)</sup> estimated the arterial wall boundaries using a conventional intensity gradient method. However, their method is significantly influenced by ultrasonic scattering in *in vivo* measurement. For the measurement of the IMT using a dynamic programming method, Liang *et al.*<sup>12)</sup> were able to detect the above boundaries precisely. However, their method requires retraining when the image characteristics change. Loizou *et al.*<sup>13)</sup> used an active contour method for carotid segmentation and IMT measurement using ultrasonic images. The disadvantage of this method is that the solution often falls into the local minima rather than into the global minima. To automatically localize boundaries and estimate the IMT, Rossi *et al.*<sup>14)</sup> proposed a novel algorithm that uses a sustain-attack filter and a multi-scale barycenter filter. The detection of MAB position performed using a sustain-attack filter requires the determination of the diameter of the artery. Thus, the near wall adventitia-media interface and far wall media–adventitia interface should be carefully positioned. However, on the near wall, echo from the adventitia-media interface overlaps with the high echo from the adventitia and reverberates from the surrounding tissue owing to the sidelobe. Therefore, the estimation of the MAB position by this method is inaccurate.

For the accurate assessment of the LIB and MAB positions, a technique using template matching between the adaptive model and the RF echo is used.<sup>15)</sup> In this technique, the assessment of the boundary positions is analyzed in the arterial longitudinal section because it provides a clearer description of the border between the lumen and the arterial wall. Moreover, in the longitudinal section, the averaging of the IMT over a short segment of the artery is applicable. However, in this method, the differences

\*E-mail address: kanai@ecei.tohoku.ac.jp

between the adaptive model and the RF echo measured *in vivo* and even those between the adaptive model and the measured reference RF echo (echo from a point scatterer) are significant. The template matching method was also reported for the accurate estimation of boundaries, but it only detects the MAB.<sup>16)</sup> To overcome and/or reduce such drawbacks, first, we consider an improved adaptive model to obtain better fitting to the reference RF echo by taking the envelope signal into account and by using a Gaussian window as an envelope function of the adaptive model. Note that an ultrasonic (US) pulse is transmitted with a Gaussian envelope,<sup>17)</sup> and that it retains its form during the propagation. In this study, applying the noninvasive ultrasonic template-matching technique, we automatically estimated the LIB and MAB positions accurately using the envelope of the improved adaptive model. To confirm the reliability of the proposed method and the accuracy of the improved adaptive model, a computer simulation of the carotid arterial wall is conducted and boundary positions are detected. Moreover, the correlation between the improved adaptive model signal and the reference RF signal and also that between their envelopes are presented and compared. In addition, we showed the comparative results between the proposed automated method and the manual method.

## 2. Principle

The structure of the arterial wall consists of three layers, i.e., the intima, media, and adventitia, which enable arteries to maintain their function and strength. The very thin intima layer consists of a single layer of endothelial cells lining the arterial wall and the media layer, which is the middle layer of the artery consisting of a complex network of smooth muscle cells, elastin, and collagen fibrils. Meanwhile, the thick adventitia layer, which is the mechanically strong outer layer, consists mainly of fibroblasts, fibrocytes, and bundles of collagen fibrils.<sup>18)</sup> These different characteristics of the respective layers produce a particular ultrasonic echo composed of reflected echoes from the LIB and MAB, as shown in the schematic view of the far-wall longitudinal section in Fig. 1. In an echo signal from the far wall, an ultrasonic echo reflected from the LIB is found, followed by a slightly low amplitude region in the media, and another echo is found around the MAB.<sup>19)</sup> Since the distance between the LIB and the MAB, which is defined as the IMT, is very small, the initial positions of the LIB and MAB should be determined accurately. Subsequently, in the present study, we modeled the echo from the arterial wall using those from the LIB and MAB. The model echoes imitated a reference echo from a glass plate.

### 2.1 Reference-RF echo

First, echoes from a glass plate are measured in a water tank, considering the depths of the glass plate from a linear transducer of 10 MHz (ALOKA UST-5410), which is connected to the modified ultrasonic diagnostic equipment (ALOKA SSD-6500), as shown in Fig. 2. The glass plate is set horizontally in the middle of the water tank, fixed by a holder that is connected to an automated XYZ stage. The depth of the carotid arterial wall from the skin differs from person to person.<sup>20)</sup> The purpose of this experiment is to confirm that the same waveforms (without taking amplitude

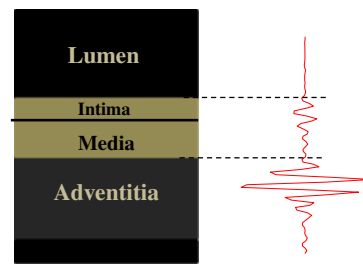


Fig. 1. (Color online) Schematic of longitudinal section of arterial wall (left) and ultrasound echo (right).

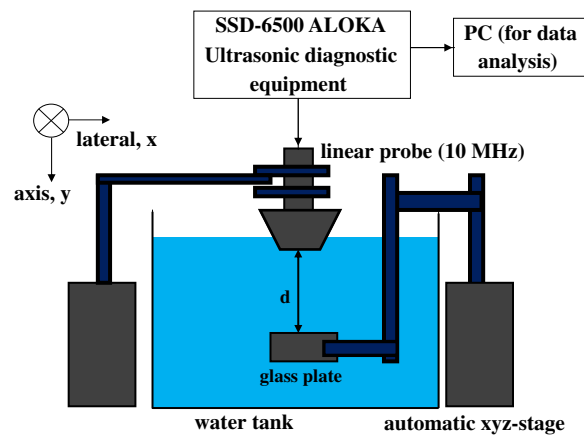


Fig. 2. (Color online) Schematic of experimental setup for measurement of echoes from glass plate (reference echo).

into account) can be obtained even at different distances from the transducer to the glass plate. Therefore, the depth denoted as  $d$  was changed by moving the glass plate in the vertical direction. Considering the typical depths of the carotid arterial wall from the skin,  $d$  was set from 13.7 to 18.7 mm at 1 mm intervals. In addition, the acoustical focus of the transducer was set at 20 mm. Figure 3 shows the amplitude-normalized RF echoes from the glass plate. To evaluate the similarity between echoes, the correlation between all the combinations of echoes is calculated. To obtain the maximum correlation coefficient between all the combinations of echoes accurately, a higher time resolution is needed. Therefore, the interpolation was applied to the echo signals before the correlation is calculated. By employing an interpolation technique,<sup>21)</sup> the maxima of correlation functions are obtained, as shown in Fig. 4. For all the calculations, the maximum values of the correlation functions exceed 0.97. From these results, it is confirmed that the waveforms of echoes can be assumed to be the same for all the different depths.

### 2.2 Optimum adaptive model

In a previous method,<sup>15)</sup> the adaptive model was fitted to the reference RF echo from a wire of 35  $\mu\text{m}$  diameter. However, there are still significant differences that would affect boundary detection. In this study, the improved adaptive model signal  $\hat{x}_i(nT_s)$  is defined by multiplying the sinusoidal wave with the Gaussian window  $w(nT_s)$ , and the envelope  $\hat{e}_i(nT_s)$  of the model signal is estimated using the Hilbert transform as

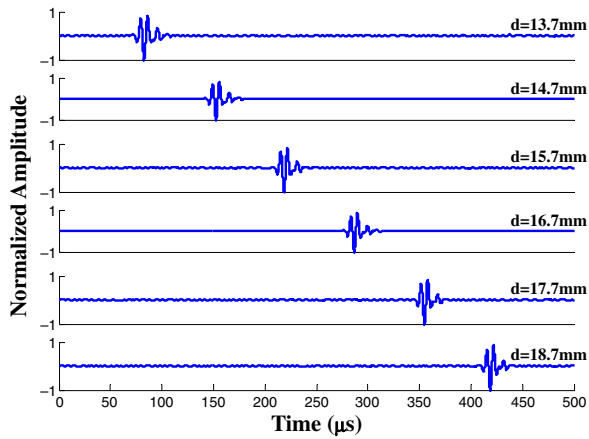


Fig. 3. (Color online) Measured glass-plate echoes at distances of 13.7, 14.7, 15.7, 16.7, 17.7, and 18.7 mm between transducer and glass plate.

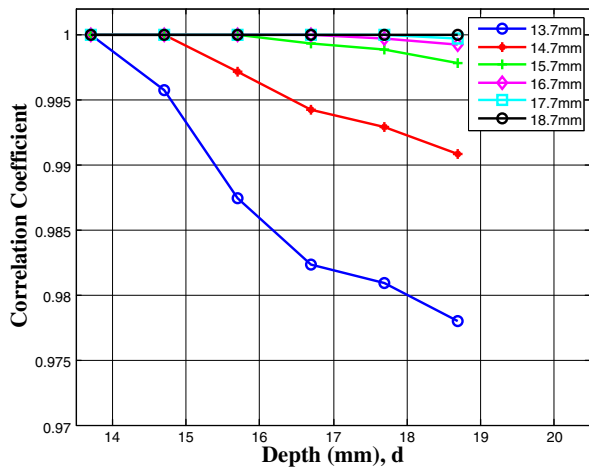


Fig. 4. (Color online) Correlation coefficients between glass-plate echoes measured at different depths.

$$\hat{e}_i(nT_s) = |Z_i(nT_s)|, \quad (1)$$

$$\hat{x}_i(nT_s) = a_i \cdot \sin[2\pi f_0(nT_s - \tau_i)] \cdot w(nT_s - \tau_i), \quad (2)$$

$$w(nT_s) = \frac{1}{\sqrt{2\pi\sigma^2}} \exp\left[-\frac{(nT_s - \mu)^2}{2\sigma^2}\right], \quad (3)$$

where  $Z_i(nT_s)$  is the analytic signal of  $\hat{x}_i(nT_s)$  obtained by the Hilbert transform,  $T_s$  is the sampling interval (sampling frequency of 40 MHz), and the center frequency  $f_0 = 7.5$  MHz is set by estimating the frequency at the maximum of power spectrum of the reference RF echo. In this paper, the reference RF echo is an echo from a glass plate shown in Fig. 3. The coefficients  $a_1$  and  $a_2$  ( $i = 1$ : LIB, 2: MAB) show their amplitude,  $\tau_1$  and  $\tau_2$  are the time delays of the LIB and MAB echoes, respectively,  $\mu$  is the central time of the model signal, and  $\sigma$  is the standard deviation of the Gaussian window  $w(nT_s)$ , which is determined so that the correlation between the envelope of improved adaptive model and the envelope of the reference RF echo is maximum. In conjunction with setting the parameter of the Gaussian window to obtain the optimum envelope of improved adaptive model, the standard deviation  $\sigma$  was used as a changeable parameter. Figure 5 shows the Gaussian windows at different standard deviations  $\{\sigma\}$ . The

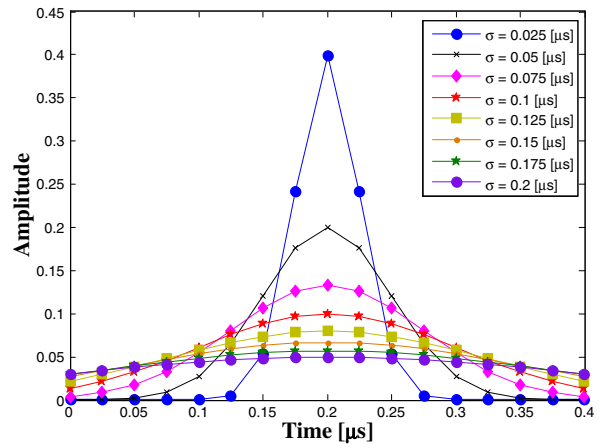


Fig. 5. (Color online) Gaussian windows at different standard deviations  $\{\sigma\}$ .

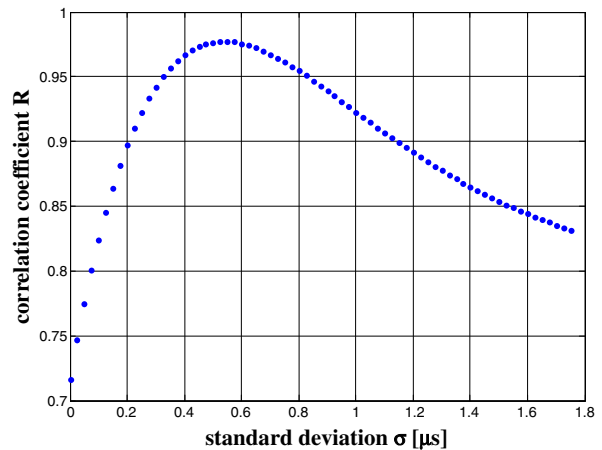
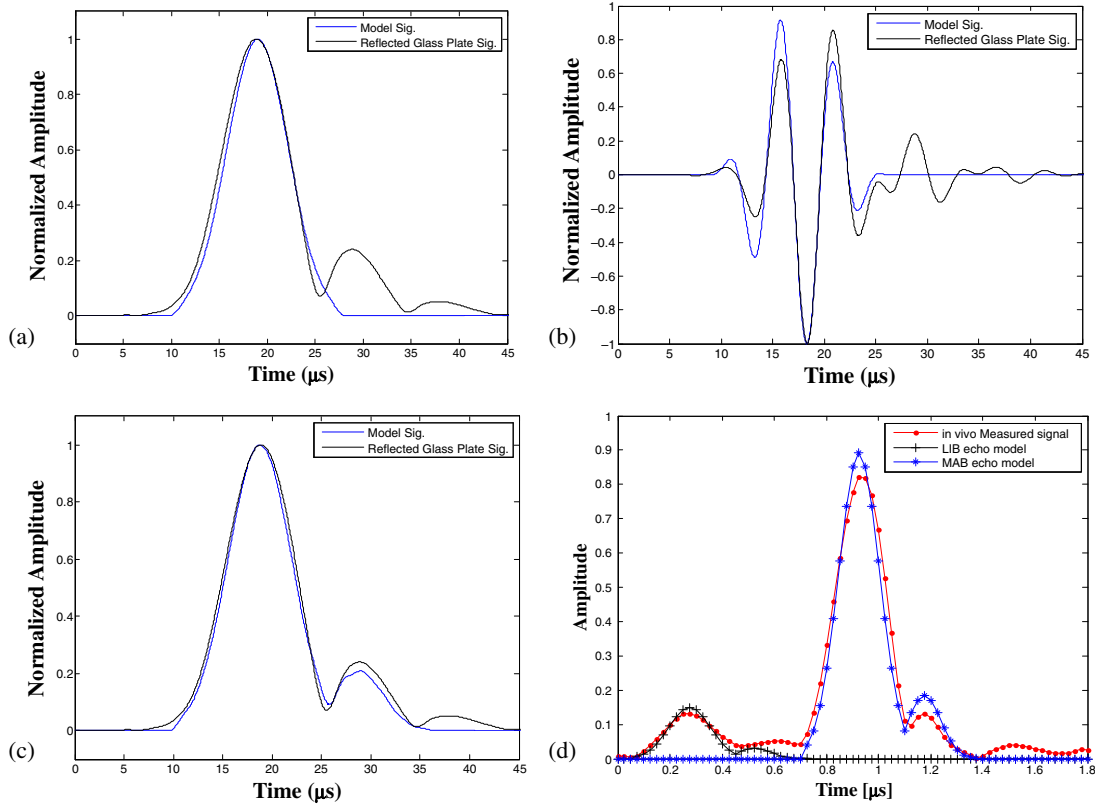


Fig. 6. (Color online) Correlation coefficients between envelopes of model echo and reference echo plotted as functions of standard deviation  $\sigma$ .

result in Fig. 6 shows that at  $\sigma$  of  $0.525 \mu s$ , the maximum correlation between the envelopes of the model and reference echoes is 0.98. In addition, the envelope  $E_r(nT_s)$  of the reference echo is also estimated by applying the Hilbert transform to the reference RF echo  $x_r(nT_s)$  expressed as

$$E_r(nT_s) = |Z_r(nT_s)|, \quad (4)$$

where  $Z_r(nT_s)$  is the analytic signal of  $x_r(nT_s)$ . Figure 7(a) shows the optimum correlation (0.98) between the envelopes of the improved adaptive model (blue line) and the envelope of the reference RF echo (black line). The correlation coefficient is 0.98, which is 7.1% higher than the maximum correlation (0.91) between the improved adaptive RF model and the reference RF echo. Also, it is 4.1% higher than the maximum correlation (0.94) between the adaptive model<sup>15)</sup> (using Hanning window) (blue line) and the reference RF echo (black line) [Fig. 7(b)]. Therefore, the envelope of the improved adaptive model should be used for the LIB and MAB echo models. However, considering the second peak (supposed to be the reverberation component) that appears in the envelope of the reference RF echo [Fig. 7(a)], the LIB and MAB echo models are constructed from the two peaks,



**Fig. 7.** (Color online) (a) Envelope of improved-adaptive model (one peak) and envelope of reference echo, (b) adaptive model and reference RF echo, (c) envelope of improved adaptive model (two peaks) and envelope of reference echo, and (d) LIB and MAB echo models and envelope of echo measured *in vivo*, which give maximum correlation coefficients.

as shown in eq. (5). The second peak overlaps with the first peak and is fixed to be  $10.5 \mu\text{s}$  [Fig. 7(c)].

$$\hat{E}_i(nT_s) = \hat{e}_i(nT_s) + \hat{e}_i(nT_s - \tau), \quad (5)$$

where  $\tau$  is the delay time of the second peak. Figure 7(c) shows the correlation between the envelope of the improved adaptive model that consists of two peaks (blue line) and the envelope of the reference RF echo (black line). The correlation coefficient is 0.99, which is higher than the maximum correlation coefficient of 0.98 between the envelope of the improved adaptive model that consists of one peak and the envelope of the reference RF echo. Therefore, the final equation of the model  $\hat{E}(nT_s)$  of an echo from the arterial wall is defined using the LIB  $\hat{E}_1(nT_s)$  and MAB  $\hat{E}_2(nT_s)$  echo models as

$$\hat{E}(nT_s) = \hat{E}_1(nT_s - \tau_1) + \hat{E}_2(nT_s - \tau_2). \quad (6)$$

Furthermore, to further confirm that the two-peak echo model is better than the one-peak echo model in boundary detection, both of the models are used and validated by simulation and *in vivo* measurement.

### 3. Simulations and Experiments

#### 3.1 Simulation experimental results

A longitudinal B-mode image of a carotid artery wall was simulated using the Field II program.<sup>22,23)</sup> To create a synthetic carotid artery wall, the parameter of the linear transducer used in the *in vivo* measurement was referred to. The transducer has 192 total elements, 96 sub elements, and a 0.2-mm-interval element pitch.<sup>24)</sup> The element height and

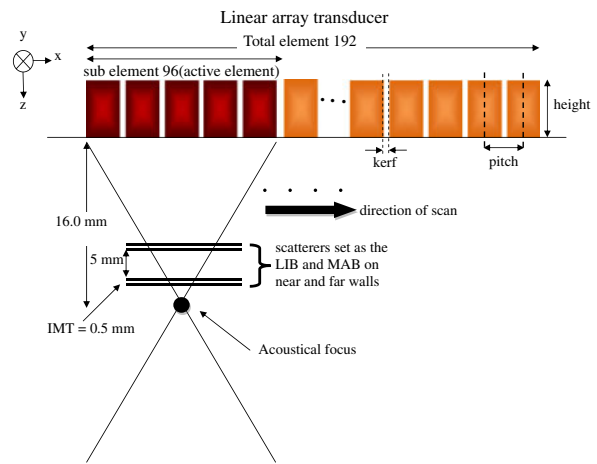


**Fig. 8.** (Color online) Schematic of linear array transducer and artery in computer simulation.

kerf were set at 6 and 0.01 mm, respectively. A boxcar window was used for apodization in both transmission and reception which had a sub aperture size of 96 elements. The acoustic focus was set at 16 mm. The excitation of the transducer consisted of three cycles of a 7.5 MHz sinusoid wave multiplied by the Gaussian window, which was the same as the improved adaptive model signal. To construct the longitudinal section, small point scatterers with  $20 \mu\text{m}$  intervals are placed at interfaces of the near and far walls, considering the typical carotid artery wall depth,<sup>20)</sup> as shown in Fig. 8. In this simulation, no attenuation is considered.

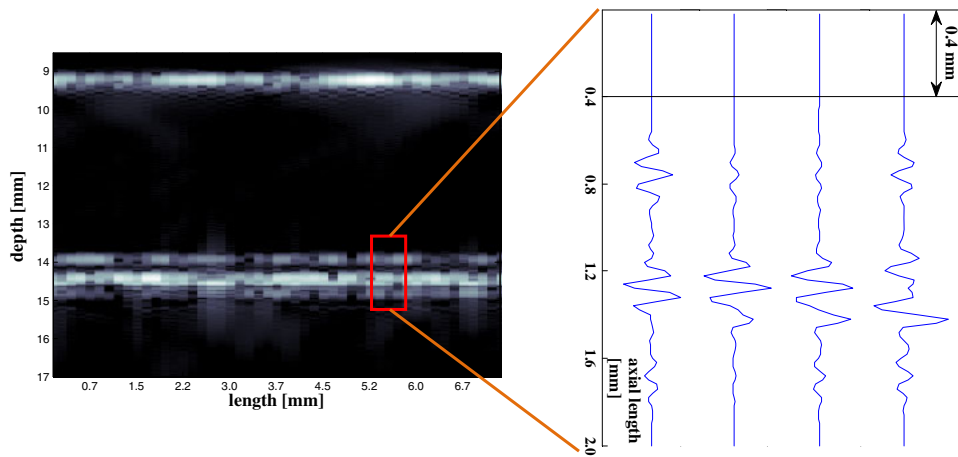


Fig. 9. (Color online) Simulated longitudinal B-mode image of carotid artery wall and RF echoes from far wall in beam of interest.

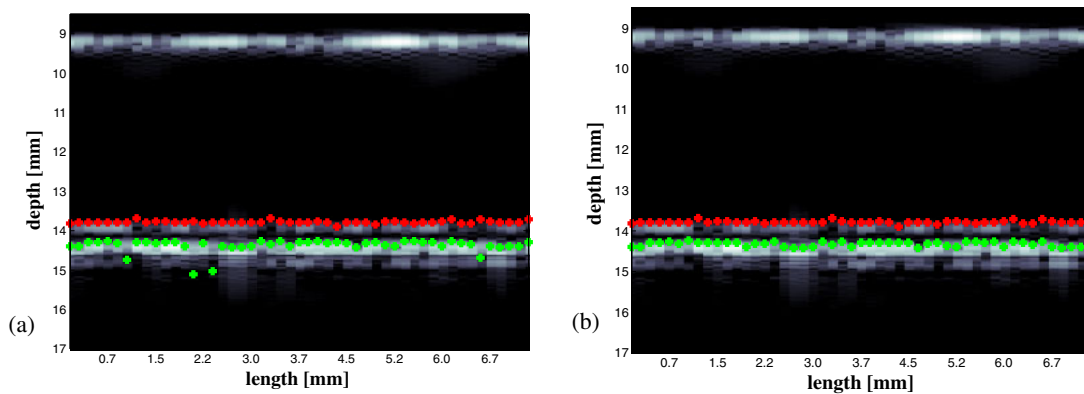


Fig. 10. (Color online) Detected boundaries with minimum errors obtained with (a) one-peak echo model and (b) two-peak echo model used in detecting LIB and MAB positions, respectively.

However, a number of scatterers are randomly placed below the adventitia layer of the far wall, which simulated the surrounding tissues at the outer parts of adventitia. The speed of sound in the tissue was set at 1540 m/s. Figure 9 shows the simulated longitudinal B-mode image of carotid arterial walls, where the electronic focus was placed on the far wall. Simulated echoes in the region surrounded by the red line in the B-mode image are shown in Fig. 9. In this study, the detection of the LIB and MAB positions is carried out using the normalized mean squared error (MSE) method, which determines the LIB and MAB so as to minimize the difference between the envelope of the improved adaptive model  $\hat{E}(nT_s)$  and the envelope of the simulated or measured signal. Let us define the envelope of the simulated echo signal as  $E_c(nT_s)$ . The RMS error  $\alpha(\tau_1, \tau_2)$  is defined as

$$\alpha(\tau_1, \tau_2) = \frac{1}{N} \frac{\sum_{n=0}^{N-1} |E_c(nT_s) - \hat{E}(nT_s; \tau_1, \tau_2)|^2}{\sum_{n=0}^{N-1} |E_c(nT_s)|^2}. \quad (7)$$

The results of the boundary detection for the simulated data are shown in Fig. 10. In Fig. 10(a), the boundaries are detected by applying the one-peak echo model of the LIB and MAB, while in Fig. 10(b) the results of the boundary

detection using the two-peak echo model of the LIB and MAB are shown. By comparing the detected boundaries (LIB: red crosses, MAB: green crosses) plotted on the simulated B-mode image of the arterial wall image in Fig. 10(a), the detected boundaries obtained using the two-peak echo model shown in Fig. 10(b) is better than those obtained by the one-peak echo model. As shown in Fig. 10(a), there are a few beams in which the MAB is misdected, especially when the one-peak echo model was used. By using the two-peak echo model, the results of these positions become closer to the MAB positions set manually [Fig. 10(b)]. In this simulation, IMT was set at 0.5 mm in a 7.2-mm-long short segment in the longitudinal direction. The estimated average IMT was 0.54 mm. The 8% error between the true and detected IMTs shows the high accuracy of the envelope of the improved adaptive model in boundary detection by the proposed method.

### 3.2 Boundary detection for *in vivo* ultrasonic data

In the *in vivo* measurement, the same modified ultrasonic diagnostic equipment (ALOKA SSD-6500) was used. The right carotid artery of a healthy male subject was scanned using a 10 MHz linear array transducer (ALOKA UST-5545), and the RF signals were sampled at 40 MHz at a 16 bit resolution. The acoustical focus of the transducer was

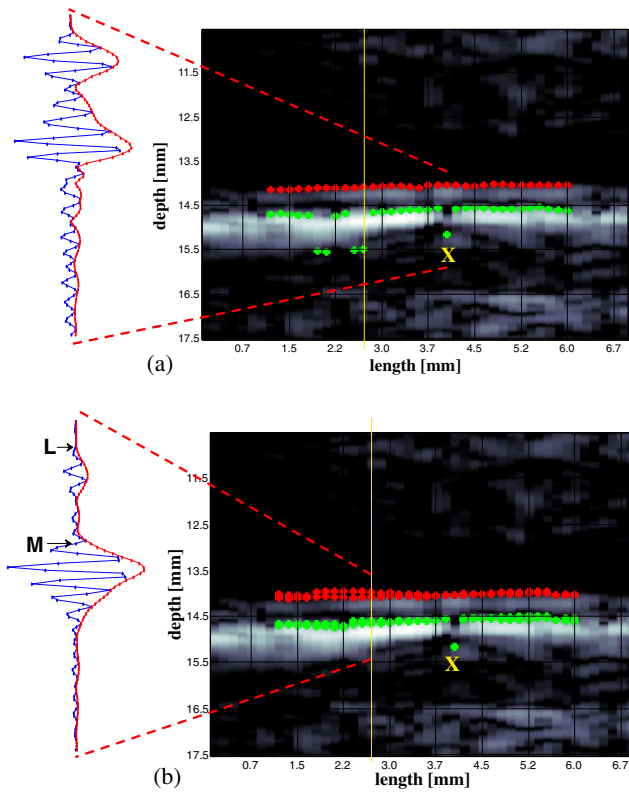


**Fig. 11.** (Color online) *In vivo* RF and envelope signals from the far wall in beam of interest and detected boundaries displayed on B-mode image. (a) Using one-peak echo model. (b) Using two-peak echo model.

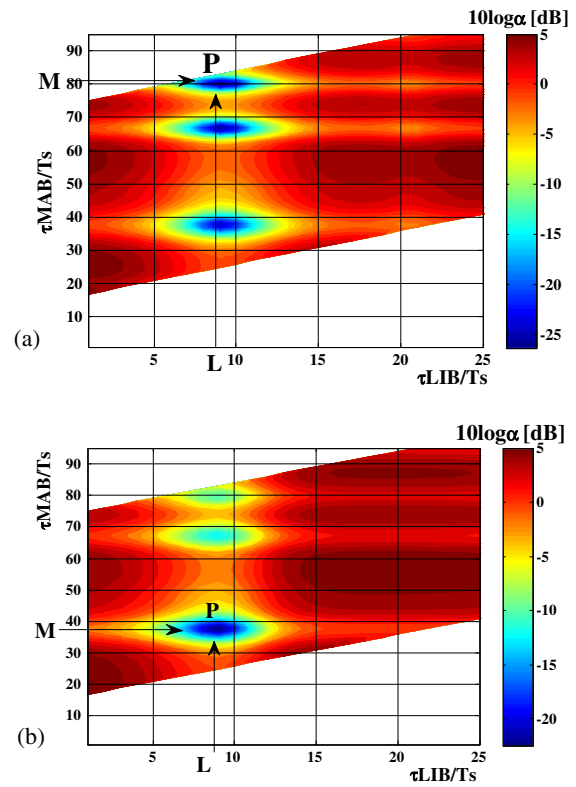


**Fig. 12.** (Color online) The error distribution  $\alpha$  in the beam of interest (indicated in Fig. 11) indicates the optimum positions of LIB and MAB (point P), marked as L and M, respectively. (a) Using one-peak echo model. (b) Using two-peak echo model.

16 mm. The minimization of the difference between the envelopes of the improved adaptive model  $\hat{E}(nT_s)$  and the envelope of the *in vivo* RF echo  $E(nT_s)$  determines the LIB and MAB positions. Since the average IMTs range from 0.5 to 1.0 mm for a healthy person<sup>25)</sup> and the IMT varies from person to person, the distance between LIB and MAB (corresponding to  $\tau_2 - \tau_1$ ) was restricted from 0.3 to 1.0 mm in the present study.

The distribution of the normalized MSE  $10 \log \alpha$  in the beam of interest [indicated in Fig. 11(b)] indicates the optimum positions of LIB and MAB (point P), marked as L and M, respectively, as shown in Fig. 12. Figure 12(a) shows the distribution of normalized MSE  $10 \log \alpha$  between the one-peak echo model and the envelope of the *in vivo* RF echo. Figure 12(b) is the normalized MSE distribution between the two-peak echo model and the envelope of the *in vivo* RF echo. For the respective distributions, the detected boundaries are plotted on B-mode images [Figs. 11(a) and 11(b)] in the beam of interest indicated by the straight line. The RF and envelope signals in the beam of interest are shown in Fig. 11(b). The detected boundaries in the *in vivo* measurement are also better when the two-peak echo model is used. The minimum  $\alpha$  of 6% at position P [Fig. 12(b)] shows that the envelope of the improved adaptive model that consists of the two peaks is in very good agreement with the envelope of the *in vivo* echo signal. The other data are also analyzed and the detected LIB (red crosses) and MAB (green crosses) are shown in Fig. 11(b). The average IMT for the short segment of 4.8 mm in the arterial longitudinal direction is 0.57 mm. However, for the

beam at position X, the detected MABs are similar between both the one- and two-peak echo models. The RF and envelope signals from the far wall at beam position X are plotted in Fig. 11(a), which corresponds to a low-SNR signal. Thus, it is confirmed that the low-SNR signal may lead to misdetection of boundaries. In addition, to further confirm the improved adaptive model and the proposed method that considered the envelope signal, Figs. 13(a) and 13(b) show the differences among the boundary positions detected by the method proposed in this study, which uses the two-peak echo model and the envelope of the *in vivo* RF echo, the manual method (from the RF signal), and the previous method, which uses the adaptive RF model and *in vivo* RF echo. The average differences between the proposed method and the manual method and between the previous method and the manual method, were 0.05 mm (blue crosses) and 0.07 mm (red crosses), respectively, for the detection of LIB positions [Fig. 13(a)]. For the detection of MAB positions [Fig. 13(b)], the differences were 0.04 and 0.08 mm, respectively.

#### 4. Discussion

In the present study, the adaptive model has been improved to detect the boundaries of IMC more accurately. From the basic experiment using a glass plate, we confirmed that similar echo signals can be obtained for typical depths of the carotid arterial wall. By the computer simulation of the carotid arterial wall, a number of scatterers are randomly placed below the adventitia layer of the far wall to simulate surrounding tissues. It is observed that, by using the two-

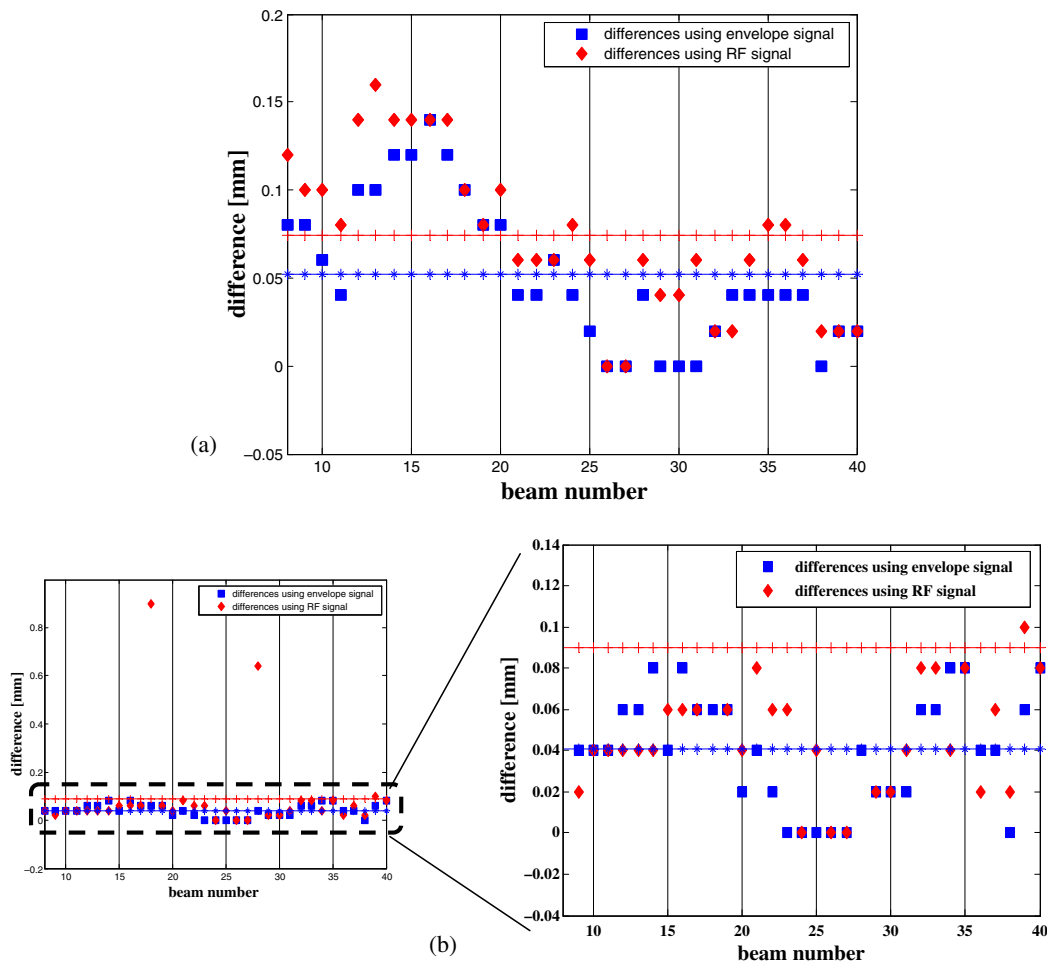


**Fig. 13.** (Color online) Differences between boundaries positions obtained by automated method (proposed method) and manual method (from RF signal) for beams of interest for (a) LIB and (b) MAB positions. Blue squares are obtained using envelope signals and red diamonds are obtained using RF signals.

**Table I.** Results obtained by the previous and proposed methods.

	RF signal <sup>a)</sup>	Previous	Proposed
		RF signal <sup>b)</sup>	Envelope signal <sup>b)</sup>
Average IMT (mm)	0.56	0.59	0.57
Minimum error distribution of beam of interest (%)	—	23	6
Average difference of LIB position from that obtained manually (mm)	—	0.07	0.05
Average difference of MAB position from that obtained manually (mm)	—	0.08	0.04

a) Manual method

b) Automated method

peak echo model, the boundary positions can be detected as shown in Fig. 10(b), with only an 8% error between the true (0.50 mm) and detected (0.54 mm) IMTs. Figure 13(a) provides an explanation of the evaluation of detected LIB positions, where the results obtained using envelope signals (blue squares) presented smaller differences than those obtained using RF signals (red diamonds). The average differences between the proposed and previous methods are listed in Table I. To clarify the MAB positions [Fig. 13(b)], as shown in Table I, the method that used envelope signals showed a smaller average difference than that using the RF signal. From the small difference between the IMT estimated by the proposed method and that determined manually and the distribution of minimized error, it is found that the proposed automated method using the improved adaptive

model (consists of two peaks) is better than the previous automated method.<sup>15)</sup>

By using the proposed template matching method, boundaries were detected automatically. To obtain a better accuracy, there are a few points that should be further investigated. In the results obtained in the present study, there were some beam positions where the MAB was misdetecting. The reason for such misdetection should be investigated. After the correction of the misdetection of the MAB, the accuracy of the proposed method should be evaluated in detail. However, the results obtained in the present study using the proposed method showed that the method is advantageous for the automatic estimation of the IMT of the carotid arterial wall, and is useful for the diagnosis of early-stage atherosclerosis.

## 5. Conclusions

In this study, we automatically estimated the boundary positions of IMT in the far wall of the carotid artery of a 4.8-mm-long short segment in the arterial longitudinal direction. The simulation of the carotid arterial wall was conducted to evaluate the accuracy of the improved adaptive model, and an 8% error between the true (0.50 mm) and detected (0.54 mm) IMTs was achieved. In the *in vivo* measurement, an average IMT of 0.57 mm was automatically estimated. From the manual method of boundary detection that was carried out by observing RF echoes, an average IMT of 0.56 mm was observed. The IMT estimated by the previous method that uses the RF echo model was 0.59 mm. From these results, it is concluded that the envelope-based two-peak echo model (improved adaptive model) proposed in the present automated method yields better results than the previous method.

- 
- 1) S. Mendis, P. Puska, and B. Norrving: *Global Atlas on Cardiovascular Disease Prevention and Control* (World Health Organization, Geneva, 2011) p. 3.
  - 2) S. S. Anand, S. Yusuf, and V. Vuksan: *Lancet* **356** (2000) 279.
  - 3) M. Tatsukawa, Y. Sawayama, N. Maeda, K. Okada, N. Furusyo, S. Kashiwagi, and J. Hayashi: *Atherosclerosis* **172** (2004) 337.
  - 4) T. A. Lakka, H. Lakka, R. Salonen, G. A. Kaplan, and J. T. Salonen: *Atherosclerosis* **154** (2001) 497.
  - 5) E. W. Rains and R. Ross: *Br. Heart J.* **69** (1993) 30.
  - 6) D. H. O'Leary: *New Engl. J. Med.* **340** (1999) 14.
  - 7) P. H. Davis, J. D. Dawson, M. B. Blecha, R. K. Masterbergen, and M. Sonka: *Ultrasound Med. Biol.* **36** (2010) 560.
  - 8) C. L. de Korte, M. Sirevogel, F. Mastik, C. Strijder, E. Velenan, G. Pasterkamp, and A. F. W. van der Steen: *Circulation* **105** (2002) 1627.
  - 9) A. Poli, E. Tremoli, A. Colombo, M. Sirtori, P. Pignoli, and R. Paoletti: *Atherosclerosis* **70** (1988) 253.
  - 10) L. Bousset, A. Serusclat, M. R. Skilton, F. Vincent, S. Bernand, P. Moulin, D. Saloner, and P. C. Douek: *J. Cardiovasc. Magn. Resonance* **9** (2007) 771.
  - 11) V. Savithri and S. Purushothaman: *Int. J. Adv. Comput. Sci. Appl.* **1** (2010) 78.
  - 12) Q. Liang, I. Wendelhag, J. Wikstrand, and T. Gustavsson: *IEEE Trans. Med. Imaging* **19** (2002) 127.
  - 13) C. P. Loizou, C. S. Pattichis, M. Pantziaris, T. Tyllis, and A. Nicolaides: *Med. Biol. Eng. Comput.* **45** (2007) 35.
  - 14) A. C. Rossi, P. J. Brands, and A. P. G. Hoeks: *Ultrasound Med. Biol.* **36** (2010) 467.
  - 15) T. Kaneko, H. Hasegawa, and H. Kanai: *Jpn. J. Appl. Phys.* **46** (2007) 4881.
  - 16) L. Fan, P. Santago, W. Riley, and D. M. Herrington: *Ultrasound Med. Biol.* **27** (2001) 399.
  - 17) L. Ferrari and J. P. Jones: *Ultrasound Med. Biol.* **11** (1985) 299.
  - 18) G. A. Holzapfel and T. C. Gasser: *J. Elasticity* **61** (2000) 1.
  - 19) A. D. M. Van Swijndregt, S. H. K. The, E. J. Gussenhoven, C. T. Lancee, H. Rijsterborgh, E. de Groot, A. F. W. van der Steen, N. Bon, and R. G. A. Ackerstaff: *Ultrasound Med. Biol.* **22** (1996) 1007.
  - 20) T. Sarkola, A. A. Abadilla, N. Chahal, E. Jaeggi, and B. W. McCrindle: *Atherosclerosis* **219** (2011) 610.
  - 21) Y. Honjo, H. Hasegawa, and H. Kanai: *Jpn. J. Appl. Phys.* **49** (2010) 07HF14.
  - 22) J. A. Jensen: *Med. Biol. Eng. Comput.* **34** (1996) Suppl. 1, Part 1, p. 351.
  - 23) I. Trots, A. Nowicki, and M. Lewandowski: *World Acad. Sci. Eng. Technol.* **64** (2010) 294.
  - 24) A. Ponnle, H. Hasegawa, and H. Kanai: *Jpn. J. Appl. Phys.* **50** (2011) 07HF05.
  - 25) S. Matsumoto: *Shinkei Cho-onpa Igaku* **19** (2006) 49 [in Japanese].